Coherent Fe-rich nano-scale perovskite oxide phase in epitaxial Sr_2FeMoO_6 films grown on cubic and scandate substrates

Hakan Deniz, Daniele Preziosi, Marin Alexe, and Dietrich Hesse

Citation: J. Appl. Phys. **121**, 023906 (2017); doi: 10.1063/1.4973878
View online: http://dx.doi.org/10.1063/1.4973878
View Table of Contents: http://aip.scitation.org/toc/jap/121/2
Published by the American Institute of Physics

Coherent Fe-rich nano-scale perovskite oxide phase in epitaxial Sr_2FeMoO_6 films grown on cubic and scandate substrates

Hakan Deniz,[1,a)] Daniele Preziosi,[1,b)] Marin Alexe,[2] and Dietrich Hesse[1]
[1]*Max Planck Institute of Microstructure Physics, Weinberg 2, D-06120 Halle (Saale), Germany*
[2]*Department of Physics, University of Warwick, Coventry CV4 7AL, West Midlands, United Kingdom*

(Received 27 October 2016; accepted 28 December 2016; published online 12 January 2017)

We report the growth of high-quality epitaxial Sr_2FeMoO_6 (SFMO) thin films on various unconventional oxide substrates, such as $TbScO_3$, $DyScO_3$, and $Sr_2Al_{0.3}Ga_{0.7}TaO_6$ (SAGT) as well as on the most commonly used one, $SrTiO_3$ (STO), by pulsed laser deposition. The films were found to contain a foreign nano-scale phase coherently embedded inside the SFMO film matrix. Through energy dispersive X-ray spectroscopy and scanning transmission electron microscopy, we identified the foreign phase to be $Sr_{2-x}Fe_{1+y}Mo_{1-y}O_6$, an off-stoichiometric derivative of the SFMO compound with Fe rich content ($y \approx 0.6$) and a fairly identical crystal structure to SFMO. The films on STO and SAGT exhibited very good magnetic properties with high Curie temperature values. All the samples have fairly good conducting behavior albeit the presence of a foreign phase. Despite the relatively large number of items of the foreign phase, there is no significant deterioration in the properties of the SFMO films. We discuss in detail how magneto-transport properties are affected by the foreign phase. *Published by AIP Publishing.* [http://dx.doi.org/10.1063/1.4973878]

INTRODUCTION

A renewed attention has been paid lately to complex magnetic oxides, especially to the ordered double perovskite Sr_2FeMoO_6 (SFMO). This material has a high Curie temperature (T_C) of ~420 K and manifests a large low-field intrinsic tunneling type magnetoresistance (LFMR) up to room temperature.[1] Band structure calculations predicted the compound to be half-metallic involving a high degree of spin polarized charge carriers (i.e., only a finite density of states at the Fermi level for the down-spin band).[2,3] These features make SFMO an attractive candidate for room temperature spintronics applications. The double-perovskite oxides have a general formula of $A_2B'B''O_6$ where A-sites are occupied by the alkaline earth cations (Sr, Ca, etc.), and B′/B″-sites are occupied by the transition metal ions (Fe, Cr, W, etc.). In SFMO, the transition metal ions on the B′/B″ sublattices order alternately, forming a NaCl-type superstructure in which each Fe^{3+} ion ($3d^5$, S = 5/2) is surrounded by six Mo^{5+} ($4d^1$, S = 1/2) ions or vice versa. This configuration results in a net magnetic moment of 4 μ_B per formula unit (f.u.) owing to the antiferromagnetic coupling of neighboring Fe and Mo ions.

Phase-pure and chemically homogeneous epitaxial thin films of this material with atomically smooth surfaces are required for the envisaged device applications in the future. The most frequently used technique for depositing thin films of SFMO is pulsed laser deposition (PLD).[4–6] However, the growth conditions for SFMO thin films are very demanding. High quality films with perfect structural order are only achieved within a limited window of growth parameters.[7] Semi-conducting films or secondary phases arise when a highly reducing or oxidizing atmosphere is used during deposition.[8–10] Therefore, Ar is the gas of choice for depositions usually.[11] The most common substrate used for SFMO growth is the cubic $SrTiO_3$ (STO) with a lattice parameter of 3.905 Å on which SFMO thin films experience a relatively small compressive strain of ~1.0%. This strain energy stored in the films grows as the film thickness increases and, when it becomes so large that relaxation becomes energetically favorable, it is released with the addition of dislocations or other structure defects in the film after a critical thickness value.[12,13] These defects impose serious limitations for technological applications since they will alter the transport/magnetic properties of SFMO films severely.

There are two major factors that deteriorate the properties of SFMO: sublattice disorder also known as the anti-site (AS) disorder and oxygen vacancies. AS disorder occurs when the site of a Fe atom is occupied by a Mo atom or vice versa. Because of the small difference between the ionic radii of Fe and Mo cations, SFMO has a natural tendency to develop the structural disorder in the B-sublattice. In turn, this leads to a reduction in the values of saturation magnetization and Curie temperature of this material because of the antiferromagnetic nature of the anti-site Fe_{Mo}-O-Fe_{Mo} bonds.[14–16] Oxygen vacancies happen abundantly in SFMO because, in most cases, the films are grown in an argon environment at elevated temperatures. Earlier studies demonstrated that, with increasing concentration of oxygen vacancies, the saturation magnetization and T_C decrease simultaneously.[17–19] Substrate induced strain is another factor that needs to be taken into account when thin films of SFMO are considered. However, some film properties can be varied effectively by utilizing the strain that results from the use of substrates with different levels of mismatch with respect to bulk SFMO. Switching of the magnetocrystalline anisotropy from an in-plane to an out-of-plane state has been

a)hdeniz@mpi-halle.mpg.de
b)Present address: Unité mixte de physique CNRS/Thales, campus de l'École polytechnique, 1, avenue Augustin-Fresnel, 91767 Palaiseau, France.

demonstrated in SFMO films by tuning the level of strain from compressive to tensile with the use of different buffer layers.[20] Strain can also be tuned by changing the thickness of films. Avoiding the relaxation of films will prevent the detrimental impacts of strain-induced defects on transport properties.

In this paper, we investigate the structure and magnetic/transport properties of SFMO films grown on various substrates which induce different levels of strain in each film. These substrates include highly atypical ones like orthorhombic $TbScO_3$ (TSO) and $DyScO_3$ (DSO) whose pseudo-cubic lattice constants closely match that of SFMO, and a newly available $Sr_2Al_{0.3}Ga_{0.7}TaO_6$ (SAGT) in addition to $SrTiO_3$. The use of SAGT results in a smaller lattice mismatch compared to STO, owing to the lattice constant of SAGT of ~3.93 Å. All films were deposited with the same growth parameters and the deposition time was kept constant for all films for comparison. The film thickness was low enough to avoid strain relaxation in the samples. X-ray diffraction (XRD) and transmission electron microscopy (TEM) were used to investigate the structure of as-grown films. Magnetic and transport properties were studied as well. We attribute the differences in respective properties to the strain state of the grown films and to the corresponding growth mode, and support this conclusion with the help of atomic structural data obtained by scanning transmission electron microscopy (STEM).

EXPERIMENTAL DETAILS

SFMO films were deposited by pulsed laser ablation of a custom-made stoichiometric target onto several different substrates: (i) cubic-STO (100) and SAGT (100), and (ii) orthorhombic-TSO (110) and DSO (110) single-crystal substrates (CrysTec GmbH, Berlin, Germany). All oxide substrates were treated appropriately to achieve atomically smooth surfaces with step-terrace formation before the depositions: (i) STO was etched in buffered HF solution and then annealed in air for 2 h at 950 °C,[21] (ii) TSO/DSO were annealed in air for 2 h at 1100 °C, and (iii) SAGT was used as received. In addition, one TSO substrate was also used as received for deposition (TSO-AR). SAGT is a new type of single-crystal oxide substrate with cubic perovskite structure. It is a solid solution of two compounds: Sr_2AlTaO_6 (SAT) and Sr_2GaTaO_6 (SGT). Following Vegard's law, the lattice parameter of a new phase can be adjusted according to the rule of mixtures using the lattice parameters of the two constituents. SAGT is composed of 70% of SGT by fraction, producing a lattice parameter of 3.931 Å. SFMO has a tetragonal structure belonging to the space group *I*4/*mmm* with the lattice constants of $a = b = 5.573$ Å and $c = 7.908$ Å.[22] SFMO grows diagonally on cubic perovskite substrates, meaning that the (110) plane of cubic substrates is parallel to the (100) plane of SFMO ($(100)_S \parallel (110)_F$) (index S—substrate; index F—film). In this case, a new unit cell for SFMO in the form of pseudo-cube can be described with a new lattice constant of 3.941 Å. Table I presents the regular and pseudo-cubic lattice constants for all the substrates as well as the lattice mismatches.

TABLE I. Lattice parameters (in Å) of all the substrates used and the misfit (in percent) between SFMO and the substrates (p.c.—pseudo cubic).

	a	*b*	*c*	a_{pc}	Misfit SFMO
STO	3.905				−0.9%
SAGT	3.931				−0.3%
DSO	5.440	5.717	7.903	3.944	0.1%
TSO	5.465	5.729	7.917	3.958	0.5%

A KrF excimer laser ($\lambda = 248$ nm) was used for all depositions. The repetition rate and laser fluence were set at 5 Hz and ~0.5 J/cm^2, respectively. All depositions were carried out using the same parameters in Ar atmosphere firing onto the ceramic target for a duration of 17 min. The substrate was held at a temperature of 750 °C, and the chamber pressure was kept at ~0.13 mbar (base pressure: $\sim 5 \times 10^{-7}$ mbar). All films were cooled down with a rate of 5 K/min under the same Ar gas pressure as they were grown. The morphology of the films was examined by a Digital Instrument D-5000 atomic force microscope (AFM). The structure and quality of the films were investigated by X-ray diffraction (XRD) using a Philips X'Pert MRD diffractometer. The atomic structure of the SFMO films was characterized by high-resolution TEM (HRTEM) and scanning TEM (STEM), using a JEOL JEM-4010 microscope at an accelerating voltage of 400 kV and a probe-corrected FEI TITAN 80–300 at 300 kV equipped with a high-angle annular dark field detector (HAADF) for Z-contrast imaging. The FEI Nova 600 Nanolab focused ion beam system was used to prepare the electron-transparent lamellas to investigate cross-sections of the films in (S)TEM. Transport properties of the samples were measured in a physical property measurement system (PPMS, Quantum Design) using the Van der Pauw method. Magnetic properties of the films were measured with a superconducting quantum interference device (SQUID, Quantum Design) magnetometer.

RESULTS AND DISCUSSION

Figure 1 shows XRD θ-2θ scans of typical SFMO films grown on all substrates. As seen from the XRD scans, the growth is highly *c*-axis oriented as evidenced by the $(002)_{pc}$ plane of SFMO films on all substrates. The full range XRD scans are absent of any spurious peaks suggesting that the films are phase-pure (supplementary material). Laue oscillations observed around the (002) film plane suggest that the SFMO films have a good crystalline quality. For all the samples, coherent film thickness was calculated using the Scherrer equation (see supplementary material). The values are 24.5 (±0.6) nm, 28.2 (±2.4) nm, 29.2 (±1.1) nm, 19.7 (±0.4) nm, and 18.8 (±0.3) nm for the films on STO, SAGT, DSO, TSO, and TSO-AR, respectively. These values indicate that the films on DSO and SAGT have the most coherent growth. Overlapping of the film and substrate peaks on DSO means that this film has the minimum value of stress among all films (inset in Fig. 1). On all substrates, based upon the XRD data, the SFMO films have some level of definite strain. The reciprocal space map (see Fig. S2) obtained

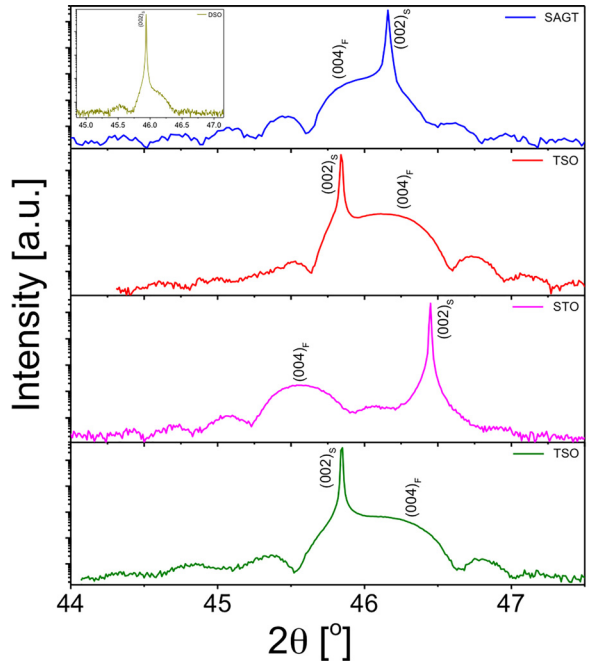

FIG. 1. Semi-log θ-2θ XRD scans of the SFMO films in the vicinity of the (002) substrate planes on the substrates (a) SAGT, (b) TSO, (c) STO, and (d) TSO (not annealed prior to the deposition). The thickness of the films is about 30 nm. Subscripts "S" and "F" refer to the substrate and the film, respectively. The inset is the θ-2θ scan for the film on DSO.

around the asymmetric (103) plane of STO showed that the SFMO film is fully strained. The measured out-of-plane lattice parameter was 3.975 Å, suggesting that the SFMO has a more tetragonal structure on STO and a more cubic one on DSO. For SAGT, DSO, TSO, and TSO-AR, the c lattice parameters were estimated to be 3 .947 Å, 3 .935 Å, 3.933 Å, and 3.932 Å, respectively, confirming strain in the films. X-ray reflectivity (XRR) measurements yielded the thicknesses of 30, 31, 30, 26, and 25 nm for the films on STO, DSO, TSO, SAGT, and TSO-AR, respectively (see Fig. S3). Film thicknesses were almost the same regardless of the strain state, except for SAGT and TSO-AR, which were not pretreated before deposition. This clearly confirms the importance of initial surface reconstruction on the growth rate of the films. Fig. S2(b) shows the AFM topography images of the SFMO films on TSO, STO, SAGT, and TSO-AR substrates, respectively (DSO not shown, being very similar to TSO). The film morphology on TSO reveals a step-terrace type structure, albeit grainy with a root-mean-squared (RMS) roughness value of 2.6 nm. The film on STO only shows a less grainy morphology with a RMS roughness of 1.7 nm with no discernible steps. The film on SAGT has a similar roughness value of 1.8 nm, but shows more pits than grains compared to the film on STO. The film grown on untreated TSO shows a very grainy morphology with a RMS roughness value of 2.1 nm.

Figure 2 displays high-resolution TEM images of SFMO films on SAGT and TSO substrates in cross-section geometry. Columnar regions showing Moiré fringes exist inside the film matrix on both samples. In most cases, they run across the entire SFMO film from the bottom interface to the top surface. They are more uniformly distributed throughout the

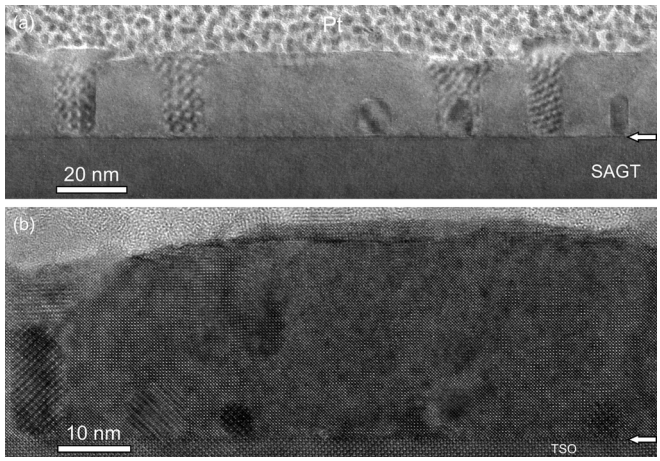

FIG. 2. (a) Overview TEM image of an SFMO film on SAGT substrate and (b) HR-TEM image of an SFMO film on TSO substrate. The white arrows point to the interface.

film matrix on SAGT substrate than they are on TSO. The films on other substrates except DSO also display similarly shaped defects inside their film matrices. On DSO, they are more irregularly shaped. Figure 3 shows the micro-structure and atomic structure of SFMO films acquired by Z-contrast imaging in STEM. We present the images of the films with the largest and the smallest lattice mismatch: one on STO and the other on DSO, respectively. In Fig. 3(a), we note the columnar-shaped areas with dark contrast that are present inside the entire SFMO film grown on STO substrate. Generally, they have a dimension of ~10 nm in width. Similar patches of dark contrast were also observed inside the SFMO film grown on DSO, mostly having spherical shapes located near the surface of the film (Fig. 3(b)). The chemistry of these columnar regions was further investigated in the STEM using EDX (energy dispersive X-ray) detector. The error was 5% for the estimation of chemical contents. EDX line scans performed across these regions showed that their contents are rich in Fe and poor in Mo (see Fig. 4). They also contain less strontium than the surrounding SFMO matrix. These results agree with the images of Fig. 3 since the intensity in Z-contrast images is sensitive to the square of atomic number. Although they are poor in Mo, these patches frequently exhibit the same lattice structure as the surrounding matrix, suggesting that these areas belong to a composition with symmetry and lattice parameters very similar to those of SFMO (Fig. 3(c)). A similar case is shown for the SFMO film on DSO in Fig. 3(d) where this nano-scale phase (NP) has a circular shape, displaying the Moiré fringes. One striking aspect observed for these regions is that there are approximately a few unit cells of regular SFMO film underneath the film/NP interface where the NP starts to form (not seen on DSO). FFT patterns were obtained from the HRTEM images for further analysis. In Fig. S4, example patterns are shown for the region of pristine film on SAGT as well as for the region containing both the NP item and the film. While the former shows that the film is strained and does not show any relaxation, the latter displays the same pattern with multiple split-reflections indicating that strain relaxation occurred inside the NP item. Careful FFT analysis

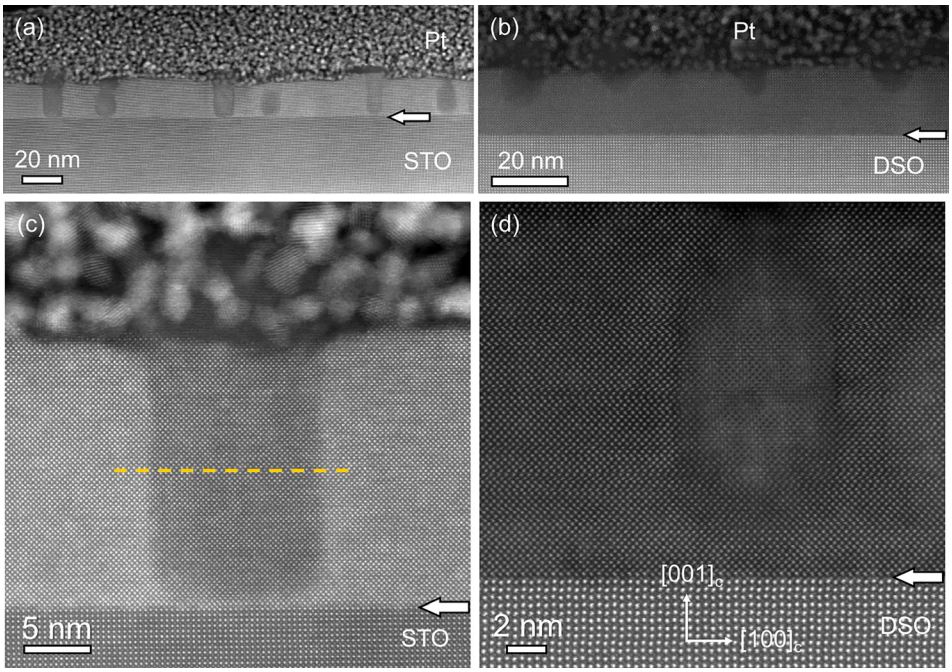

FIG. 3. (a) Overview STEM image of an SFMO film on STO substrate; [100] zone axis. (b) Overview image of an SFMO film on DSO substrate. (c) High-resolution HAADF-STEM image of an SFMO film showing a NP item (poor in Mo content) embedded coherently inside the SFMO film matrix. The broken orange line shows where an EDX line scan was acquired, (d) HR-STEM image of an SFMO film on DSO, showing a sharp interface and a round-shaped NP item exhibiting Moiré fringes. The white arrows point to the interface.

reveals that there are several dislocations existing at the interface between the NP item and SFMO matrix (see Fig. S4(d)). This suggests that the NP items might play a crucial role in relieving the stress in the films at the early stage of the growth. Once the nucleation takes place for the NP items, the growths of SFMO and the NP continue simultaneously. The strain relaxation results in the changing of lattice spacings slightly inside the NP with respect to those of the surrounding SFMO, hence, leading to the appearance of Moiré fringes. These are interference patterns formed by superposition of two sets of crystal planes when they are rotated a few degrees with respect to one another or when they have different periodicities/lattice constants. The former is called the rotational Moiré and the latter is the translational Moiré. Although they could be useful for investigation of interfaces and defects, care needs to be taken in their interpretation. Since they are the result of interference effects, they appear the same even if two crystals are not in contact.[23]

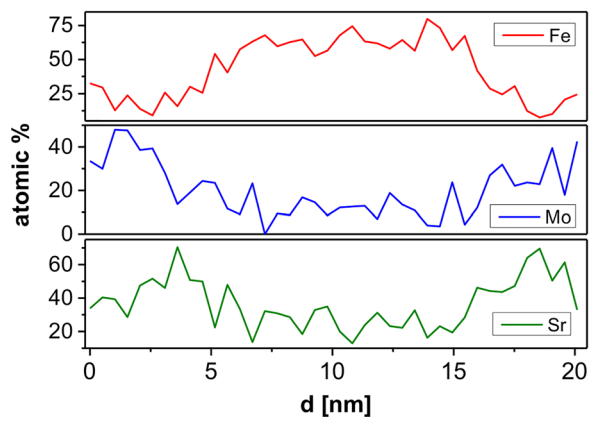

FIG. 4. Plotted atomic percentages of (a) Fe, (b) Mo, and (c) Sr across a nano-sized phase obtained through EDX analysis. The error in composition estimation is 5%.

These dark regions are most likely to correspond to some off-stoichiometric $Sr_{2-x}Fe_{1+y}Mo_{1-y}O_6$ (SFO) phase with Fe-rich content ($y \approx 0.6$). The compound $SrFe_{0.75}Mo_{0.25}O_{3-\delta}$ belonging to the space group $I4/mcm$ ($a = 5.543$ Å, $c = 7.847$ Å) is the closest candidate for the SFO.[24] Similarly, we have more iron and less molybdenum even though the exact stoichiometry is not the same. However, it might be still feasible to stabilize such an off-stoichiometric phase inside the SFMO matrix, resembling a solid-state solution while keeping the structure the same. This may explain the coherent placement of this nano-scale phase inside the SFMO matrix, if we consider that SFO has a tetragonal symmetry with lattice constants similar to those of SFMO. The density of these regions was estimated to be ~10% by volume on STO from FIB lamellae using HAADF-STEM images. Since the SFO regions have a very similar lattice structure as SFMO, it is impossible to distinguish them from each other in XRD scans despite the high number of the nano-phase items.

Magnetic properties were investigated for the films grown on STO and SAGT substrates. Hysteresis loops M(H) were acquired at 50 K with the field strength up to 4 T along the [100] direction of the substrates. Magnetization versus temperature data M(T) were acquired with an applied magnetic field of 0.5 T along the [100] directions. A field cooling (FC) condition with an applied field value of 4 T was realized. Figure 5 shows the M(H) curves for both films. The inset in Fig. 5 shows that both films have similar values of the coercive field. The saturation magnetization of the film grown on STO substrate is about 120 emu/cm^3 whereas for the film on SAGT, this value becomes ~150 emu/cm^3. This result gave us the opportunity to consider the SFMO film completely saturated at the applied field value of 4 T. Hence, the subtraction of the diamagnetic contribution of the substrates from the M(T) curves has been performed by removing, from the measured M(T) curves, the values of the slope, calculated at high field for the M(H) curve, multiplied by

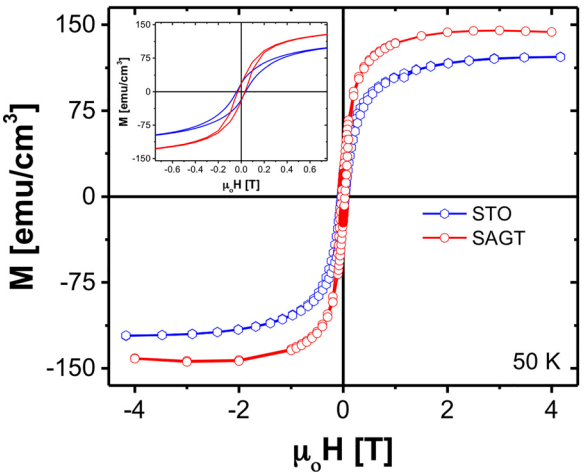

FIG. 5. Hysteresis loops M(H) for SFMO films on STO (blue) and SAGT (red) substrates at 50 K. The inset shows the magnified view of the low-field region. Both films have similar values of the coercive field.

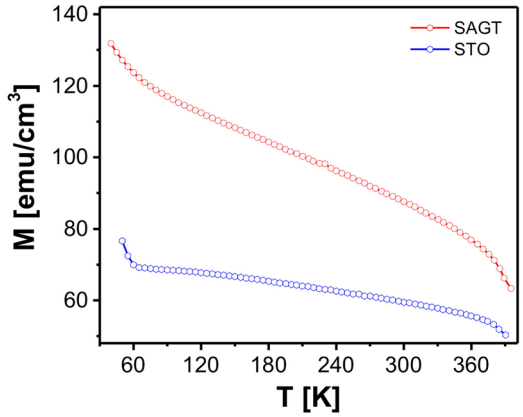

FIG. 6. Magnetization versus temperature M(T) curves for SFMO films on STO (blue) and SAGT (red) substrates at 0.5 T.

0.5 T. Figure 6 shows the result of such an operation, and it is striking to note that the value of magnetization does not go to zero around 400 K indicating a pretty high Curie temperature for both SFMO films grown onto STO and SAGT substrates. The linear extrapolation of the high-temperature part of the M(T) data yields a Curie temperature of ~390 K for the film on STO and ~415 K for the film on SAGT. The measured T_C values imply roughly 10% and 1.5% of AS defect concentrations in the B-sublattice for the films on STO and SAGT, respectively, following the argument of Ogale *et al.* that the Curie temperature decreases at a rate of 3 K per percent AS defect content.[17] For the film on SAGT, this value is not so high, considering the rather low deposition temperature of the film. Unfortunately, we could not measure the magnetic properties of the films grown on DSO/TSO substrates in our magnetometer because of the very large paramagnetic contribution of these substrates. For the film on STO, hysteresis loops were obtained at several different temperatures ranging from 2 K up to 370 K (Fig. S5 in the supplementary material). The plot of saturation magnetization versus temperature shows that the M_S values have an anomalous behavior at around 50–60 K agreeing with the M(T) curves in Fig. 6, and the magnetization increases further as the temperature decreases instead of reaching the saturation state. The transition that is seen at around 50 K might be attributed to the Curie temperature of the second phase in the SFMO matrix. The upturn below 50 K suggests that there might exist a ferromagnetic coupling between the magnetizations of the SFMO film and nano-scale phase, resulting in higher M_S values at low temperatures.

Figure 7(a) shows resistivity versus temperature curves acquired for all the films with an applied magnetic field value of 0 T and 2 T. The film on DSO has the lowest resistivity whereas the film on STO has the highest one with the exception of the film grown on the untreated TSO substrate. All

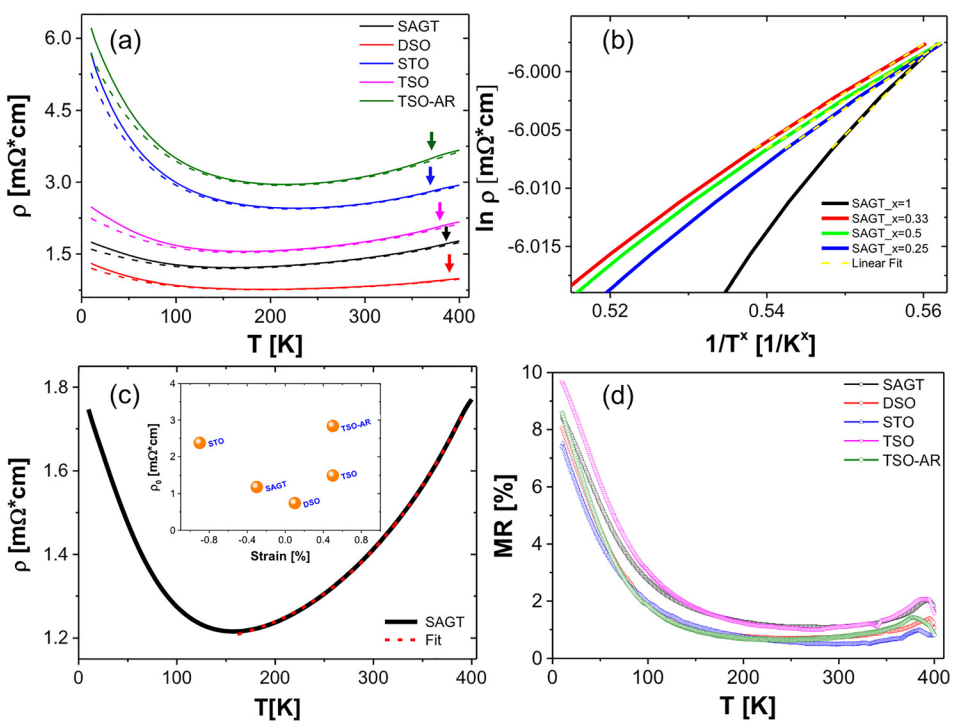

FIG. 7. (a) Resistivity ρ versus temperature curves for the SFMO films on STO, DSO, TSO, and SAGT substrates at zero magnetic field (solid lines) and at a field of 2 T (dashed lines). The arrows point to the anomaly seen in the high-temperature region of the resistivity. (b) The plot of $ln\rho$ versus $1/T^x$ for the film on SAGT for the semiconducting region below T_{min}. The dashed yellow lines are the linear fits for each possible x-value. (c) Plot of resistivity versus temperature for the film on SAGT and the fitted curve (dashed red) for the metallic regime above T_{min}. The inset shows the plot of the residual resistivity values versus the level of the strain state. (d) Temperature dependent magnetoresistance (MR) curves of all the films from (a).

samples display a metallic behavior all the way down to a transition temperature T_{min}, after which the resistivity increases continuously with decreasing temperature. T_{min} was simply estimated as the value at which the temperature derivative of the resistivity curve (i.e., $d\rho/dT$) was crossing the T-axis. The slight anomaly observed in the high temperature region of the resistivity curves (see, for example, the arrows in Fig. 7(a)) is most probably linked to the paramagnetic to ferromagnetic transition of the films occurring at T_{trans}. These were estimated from the rather broad peaks observed in the $d\rho/dT$ curves. The T_{min} and T_{trans} values are listed in Table II, and while T_{trans} presents a clear strain-dependence, i.e., the lowest value for the largest strain irrespective of the sign, the T_{min} values do not seem to follow the same trend, most likely due to the presence of the aforementioned nano-scale phase items in the films. Indeed, the less itinerant character of charge carriers for temperatures lower than T_{min} can be interpreted as the consequence of localization effects akin to the disorder induced by the NP items.[25] In this picture, the quasi-particles are thought to hop between localized states in a so-called variable range hopping (VRH) regime. In this relatively low temperature region, the resistivity curves can be expressed through a relation proportional to $exp(T_0/T)^{1/(d+1)}$ with T_0 being a constant depending upon the density of states at the Fermi level and upon the radius of the localized states, and d representing the spatial dimension in which the transport takes place. Moreover, as reported by Saloaro *et al.*,[26] the observed upturn can be modeled through a pure thermally activated mechanism with the resistivity proportional to $exp(E_a/K_bT)$, with E_a and K_b being the activation energy and the Boltzmann constant, respectively. Thus, in order to distinguish between the different conduction mechanisms, i.e., VRH and/or thermally activated, for temperatures lower than T_{min}, the $ln\rho$ *vs.* $1/T$ or $(1/T)^{1/(d+1)}$ plots should render a straight line. Figure 7(b) shows this kind of plot for all the possible 1/T dependencies for the SFMO grown onto SAGT substrate. It is worth noting that in the low temperature region, away from the transition, a linear fit is capable to well reproduce the data for all the $1/T$-dependencies. This result also holds for the other different strain states. As a result, the experimental data at temperatures below T_{min} cannot be reproduced in an unequivocal way, and the different mechanisms can be easily confused. For this reason, we concentrated on the high temperature region even though more accurate fitting procedures are on the way and will be presented in a dedicated paper.

In the metallic T-regime (above T_{min}), the best fit to the temperature dependence of the resistivity curves can be achieved with the formula $\rho(T) = \rho_0 + AT^{\alpha}$, where the constant ρ_0 is related to T-independent impurity scattering, and the AT^{α} term represents the mix between different scattering processes, i.e., the electron-electron (T^2), the single magnon (T^3), two magnons ($T^{4.5}$), the acoustic phonons (T^5), and finally the spin-waves ($T^{3.5}$) scattering mechanisms.[27] In Fig. 7(c), a representative resistivity plot (SFMO/SAGT) is shown with the fitted curve which models, with a high accuracy, the experimental data, the coefficient of determination R^2 almost being 1. The parameters ρ_0, A, α, and R^2 are listed in Table III for all the films. It appears more clear that the resistivity values are strongly correlated with the strain level that exists in each film as can be easily inferred from the inset of Fig. 7(c) where the residual resistivity values obtained from the fitting procedure are plotted as a function of the strain states. The ρ_0 values can be considered as a check of the film quality, and the best value is obtained from thin films that manifest an almost zero-degree of strain and, when this is increased irrespective of the sign, the residual resistivity increases. The latter can be linked to the presence of the NP items as already ascertained by the TEM data for thin films with a high level of strain. When the strain energy becomes too large, it relaxes and favors the defect and, hence, deteriorates the transport properties. The resistivity values measured for our films are similar, but a bit higher compared to the reported values before,[28–30] which is understandable considering the presence of the NP items.

Magnetoresistance (MR) curves as a function of temperature obtained through the formula $[\rho\ (H=0) - \rho\ (H)]/\rho\ (H=0)$, are shown in Fig. 7(d). The MR ratio of the films shows peaks at high temperatures; in this respect, it agrees with the previous results observed for colossal magnetoresistance oxides where such maximums on *MR vs. T* are typically seen in the area of the ferromagnetic-paramagnetic transition.[31] This confirms that all films have Curie temperature values around or above 400 K, which is in qualitative agreement with the T_{trans} values reported in Table II. The MR curves here exhibit rather narrow small peaks unlike those of the doped manganites.[32] Interestingly, the MR values of the films on SAGT and TSO are higher than those of the films on other substrates at all range of temperatures. For the films on other substrates, the MR curves cross each other at several points over the whole temperature range. The MR values of the films are very low and usually less than 2% at room temperature. An increase of the MR signal is observed in the low temperature region where the quasi-particles experience a field-dependent decrease of the localization effect induced most probably by the presence of the NP items. Additional studies are under way to completely elucidate

TABLE II. T_{min} and T_{trans} values with corresponding misfits.

	T_{min}	T_{trans}	Misfit SFMO
STO	227	370	−0.9%
SAGT	157	388	−0.3%
DSO	192	393	−0.1%
TSO	173	380	0.5%
TSO-AR	215	371	0.5%

TABLE III. Parameters for the resistivity fits for each SFMO film.

	Misfit SFMO	ρ_0 (mΩ cm)	A (mΩ cm $K^{-\alpha}$)	α	R^2
STO	−0.9%	2.4	4.25×10^{-13}	4.7	0.99948
SAGT	−0.3%	1.2	1.49×10^{-9}	3.3	0.99995
DSO	−0.1%	0.7	1.62×10^{-11}	3.9	0.99999
TSO	0.5%	1.5	3.07×10^{-10}	3.6	0.99998
TSO-AR	0.5%	2.9	3.50×10^{-12}	4.4	0.99949

this, but for the moment this is beyond the scope of this paper.

CONCLUSION

We investigated the structure and properties of epitaxial SFMO films grown on substrates with different levels of mismatch. We demonstrated that SFMO films can grow on orthorhombic substrates as well as they do on cubic ones. We observed the presence of a nano-scale phase (NP) coherently embedded inside the film matrix. This new NP has approximately a chemical composition of $Sr_{2-x}Fe_{1+y}Mo_{1-y}O_6$, resembling the known $SrFe_{0.75}Mo_{0.25}O_{3-\delta}$ compound in terms of the structure and exists coherently as a nano-phase inside the SFMO film matrix. Full range θ-2θ XRD scans did not reveal any spurious peaks. Together with the STEM results, this fact suggests that the NP has a crystal structure very similar to that of SFMO, and the SFO/SFMO system is pretty close to a solid solution since the structure and composition of the SFMO matrix remain unchanged. The SFMO films in general have a good quality, implying that the deposition parameters were properly optimized to obtain in overall, a good stoichiometry transfer from the target towards the substrate. We believe that inhomogeneities in the target might result in the formation of the foreign nano-phase which is then stabilized by the substrate-induced strain. This must be the reason for mostly the regular appearance of this nano-phase on all the substrates except DSO, whose use leads to almost no strain in the film. Moreover, PLD being a very complex non-equilibrium process, the observed off-stoichiometry in the SFMO thin films might also be induced by a scarce control of the thermodynamic stability of the laser-induced plume. The large number of the NP items is akin to a substantial deterioration in the transport properties of the SFMO films. As a consequence, the films indeed show an upturn of resistivity at relatively low temperatures. However, we still observe high Curie temperatures and reasonably good magnetization values for the films on STO and SAGT. Although the lattice constant of SAGT does not perfectly match that of SFMO, it does not result in deleterious effects as in the case of scandate substrates in probing the magnetic properties of the films. The film on SAGT has better magnetic properties as well as better conductivity and MR behavior compared to the film on STO. Unfortunately, we cannot make a comparison for the magnetic properties with other films due to the inability of obtaining any meaningful measurements on scandate substrates. The transport properties of our films are highly dependent upon the strain; the lesser the strain level is, the better the conductivity is in our films. For future efforts, growth techniques that maintain the strain and the defects at minimum in SFMO films will pave the way for device applications.

SUPPLEMENTARY MATERIAL

See supplementary material for the detailed XRD characterization, AFM morphology data, the application of Scherrer equation for coherent thickness estimation, XRR analysis for thickness determination, FFT analysis of HRTEM image of the film on SAGT, and the additional hysteresis loops for the film on STO.

ACKNOWLEDGMENTS

We thank Mr. Norbert Schammelt for the FIB-based TEM sample preparation of our SFMO samples, Dr. Xavi Marti for his help on X-ray reflectivity measurements, and Mr. Tianping Ma for helpful discussions.

[1]K.-I. Kobayashi, T. Kimura, H. Sawada, K. Terakura, and Y. Tokura, "Room-temperature magnetoresistance in an oxide material with an ordered double-perovskite structure," Nature **395**, 677–680 (1998).
[2]T. Saitoh, M. Nakatake, A. Kakizaki, H. Nakajima, and O. Morimoto, "Half-metallic density of states in Sr_2FeMoO_6 due to Hund's rule coupling," Phys. Rev. B **66**, 035112 (2002).
[3]M. Bibes, K. Bouzehouane, A. Barthelemy, M. Besse, and S. Fusil, "Tunnel magnetoresistance in nanojunctions based on Sr_2FeMoO_6," Appl. Phys. Lett. **83**, 2629–2631 (2003).
[4]H. Asano, S. Ogale, J. Garrison, A. Orozco, and Y. Li, "Pulsed-laser-deposited epitaxial Sr_2FeMoO_{6-y} thin films: Positive and negative magnetoresistance regimes," Appl. Phys. Lett. **74**, 3696–3698 (1999).
[5]T. Manako, M. Izumi, Y. Konishi, K. Kobayashi, and M. Kawasaki, "Epitaxial thin films of ordered double perovskite Sr_2FeMoO_6," Appl. Phys. Lett. **74**, 2215–2217 (1999).
[6]H. Yin, J. Zhou, R. Dass, and J. McDevitt, "Intra-versus intergranular low-field magnetoresistance of Sr_2FeMoO_6 thin films," Appl. Phys. Lett. **75**, 2812–2814 (1999).
[7]W. Westerburg, D. Reisinger, and G. Jakob, "Epitaxy and magnetotransport of Sr_2FeMoO_6 thin films," Phys. Rev. B **62**, R767–R770 (2000).
[8]M. Besse, F. Pailloux, A. Barthelemy, K. Bouzehounane, and A. Fert, "Characterization methods of epitaxial Sr_2FeMoO_6 thin films," J. Cryst. Growth **241**, 448–454 (2002).
[9]D. Sanchez, M. G. Hernandez, N. Auth, and G. Jakob, "Structural, magnetic, and transport properties of high-quality epitaxial Sr_2FeMoO_6 thin films prepared by pulsed laser deposition," J. Appl. Phys. **96**, 2736–2742 (2004).
[10]D. Kim, J. Kim, B. Park, and J. Lee, "$SrFeO_3$ nanoparticles-dispersed $SrMoO_4$ insulating thin films deposited from Sr_2FeMoO_6 target in oxygen atmosphere," Appl. Phys. Lett. **84**, 5037–5039 (2004).
[11]S. Shinde, S. Ogale, R. Greene, T. Venkatesan, and K. Tsoi, "Thin films of double perovskite Sr_2FeMoO_6: Growth, optimization, and study of the physical and magnetotransport properties of films grown on single-crystalline and polycrystalline $SrTiO_3$ substrates," J. Appl. Phys. **93**, 1605–1612 (2003).
[12]T. Fix, D. Stoeffler, S. Colis, C. Ulhaq, and G. Versini, "Effects of strain relaxation on the electronic properties of epitaxial Sr_2FeMoO_6 grown by pulsed laser deposition on $SrTiO_3$ (001)," J. Appl. Phys. **98**, 023712 (2005).
[13]M. Saloaro, H. Deniz, H. Huhtinen, H. Palonen, S. Majumdar, and P. Paturi, "The predominance of substrate induced defects in magnetic properties of Sr_2FeMoO_6 thin films," J. Phys.: Condens. Matter **27**, 386001 (2015).
[14]Y. Huang, M. Karppinen, H. Yamauchi, and J. Goodenough, "Systematic studies on effects of cationic ordering on structural and magnetic properties in Sr_2FeMoO_6," Phys. Rev. B **73**, 104408 (2006).
[15]J. Navarro, L. Balcells, F. Sandiumenge, M. Bibes, and A. Roig, "Antisite defects and magnetoresistance in Sr_2FeMoO_6 double perovskite," J. Phys.: Condens. Matter **13**, 8481–8488 (2001).
[16]D. Sanchez, J. Alonso, M. Hernandez, M. M. Lope, and J. Martinez, "Origin of neutron magnetic scattering in antisite-disordered Sr_2FeMoO_6 double perovskites," Phys. Rev. B **65**, 104426 (2002).
[17]A. Ogale, S. Ogale, R. Ramesh, and T. Venkatesan, "Octahedral cation site disorder effects on magnetization in double-perovskite Sr_2FeMoO_6: Monte Carlo simulation study," Appl. Phys. Lett. **75**, 537–539 (1999).
[18]C. Frontera and J. Fontcuberta, "Configurational disorder and magnetism in double perovskites: A Monte Carlo simulation study," Phys. Rev. B **69**, 014406 (2004).
[19]Q. Zhang, Z. F. Xu, L. F. Wang, S. H. Gao, and S. J. Yuan, "Structural and electromagnetic properties driven by oxygen vacancy in $Sr_2FeMoO_{6-\delta}$ double perovskite," J. Alloys Compd. **649**, 1151–1155 (2015).

[20]C. Du, R. Adur, H. Wang, A. Hauser, F. Yang, and P. C. Hammel, "Control of magnetocrystalline anisotropy by epitaxial strain in double perovskite Sr_2FeMoO_6 films," Phys. Rev. Lett. **110**, 147204 (2013).
[21]G. Koster, B. Kropman, G. Rijnders, D. Blank, and H. Rogalla, "Quasi-ideal strontium titanate crystal surfaces through formation of strontium hydroxide," Appl. Phys. Lett. **73**, 2920–2922 (1998).
[22]S. Kim, B. Lee, and C. Kim, "Neutron and Mossbauer studies of the double perovskite A_2FeMoO_6 (A = Sr and Ba)," J. Magn. Magn. Mater. **242–245**, 747–750 (2002).
[23]D. B. Williams and C. B. Carter, *Transmission Electron Microscopy: A Textbook for Materials Science* (Springer, New York, 2009).
[24]M. Retuerto, M.-R. Li, Y. B. Go, A. Ignatov, M. Croft, K. V. Ramanujachary, J. Hadermann, J. P. Hodges, R. H. Herber, I. Nowik, and M. Greenblatt, "Magnetic and structural studies of the multifunctional material $SrFe_{0.75}Mo_{0.25}O_{3-\delta}$," Inorg. Chem. **51**, 12273–12280 (2012).
[25]N. F. Mott and E. A. Davis, *Electronic Processes in Non-Crystalline Materials* (OUP, Oxford, 2012).
[26]M. Saloaro, S. Majumdar, H. Huhtinen, and P. Paturi, "Absence of traditional magnetoresistivity mechanisms in Sr_2FeMoO_6 thin films grown on $SrTiO_3$, MgO and $NdGaO_3$ substrates," J. Phys.: Condens. Matter **24**, 366003 (2012).
[27]S. Mercone, C. Perroni, V. Cataudella, C. Adamo, and M. Angeloni, "Transport properties in manganite thin films," Phys. Rev. B **71**, 064415 (2005).
[28]R. Borges, S. Lhostis, M. Bari, J. Versluijs, and J. Lunney, "Thin films of the double perovskite Sr_2FeMoO_6 deposited by pulsed laser deposition," Thin Solid Films **429**, 5–12 (2003).
[29]J. Rager, A. Berenov, L. Cohen, W. Branford, and Y. Bugoslavsky, "Highly aligned, spin polarized thin films of Sr_2FeMoO_6 by a chemical vapor process," Appl. Phys. Lett. **81**, 5003–5005 (2002).
[30]S. Wang, H. Pan, X. Zhang, G. Lian, and G. Xiong, "Double-perovskite Sr_2FeMoO_6 epitaxial films with ordered cation structure grown in mixture gas of hydrogen and argon," Appl. Phys. Lett. **88**, 121912 (2006).
[31]J. Coey, M. Viret, and S. von Molnar, "Mixed-valence manganites," Adv. Phys. **48**, 167–293 (1999).
[32]X. Hong, J. D. Hoffman, C. H. Ahn, and Y. Bason, "Effect of electric field doping on the anisotropic magnetoresistance in doped manganites," Phys. Rev. B **74**, 174406 (2006).